

Article

Study on the Solid Production Mechanism of the Fractured Granite Reservoirs-Example of YL Area in Qiongdongnan Basin

Xiongdi Zuo ¹, Tao Wang ², Lanling Shi ², Lei Lei ², Jian Wu ², Liangbin Dou ¹ and Tiantai Li ^{1,*}¹ School of Petroleum Engineering, Xi'an Shiyou University, Xi'an 710065, China² Shanghai Branch of CNOOC Ltd., Shanghai 200335, China

* Correspondence: ttli@xsyu.edu.cn; Tel.: +86-13909204378

Abstract: The granite buried hill gas reservoir in YL area of Qiongdongnan basin faces a serious problem of solid production, which seriously affects gas well production and reduces economic benefits; however, the solid production mechanism of fractured granite reservoirs is still unclear. In this study, the reasons for solid production were revealed and the mechanism was clarified based on the analysis of geological and mechanical characteristics of the granite buried hill reservoir. The solid production of fractured granite reservoirs can be divided into three modes, those being shedding of fracture filling and solid particles on the fracture wall, shear slip failure along the fracture, and shear failure of granite matrix. Take the YL area in the Qiongdongnan Basin as an example, the solid production of fractured granite reservoirs is mainly based on shedding of fracture filling and solid particles on the fracture wall and shear slip failure along the fracture, the possibility of shear failure of granite matrix is less. In addition, the closer the wellbore, the greater the risk of shedding of fracture filling and solid particles on the fracture wall. The high-angle fractures have a greater risk of shear slip failure. In addition, the direction of the minimum horizontal principal stress is higher risk of solid production. The research provides the basis and foundation for safe and efficient development of fractured granite reservoirs and for later measure selection and optimization.

Keywords: granite buried hill reservoir; fractured reservoir; solid production; fracture filling; shear slip; fracture



Citation: Zuo, X.; Wang, T.; Shi, L.; Lei, L.; Wu, J.; Dou, L.; Li, T. Study on the Solid Production Mechanism of the Fractured Granite Reservoirs-Example of YL Area in Qiongdongnan Basin. *Processes* **2022**, *10*, 2556. <https://doi.org/10.3390/pr10122556>

Academic Editor: Yidong Cai

Received: 7 November 2022

Accepted: 28 November 2022

Published: 1 December 2022

Publisher's Note: MDPI stays neutral with regard to jurisdictional claims in published maps and institutional affiliations.



Copyright: © 2022 by the authors. Licensee MDPI, Basel, Switzerland. This article is an open access article distributed under the terms and conditions of the Creative Commons Attribution (CC BY) license (<https://creativecommons.org/licenses/by/4.0/>).

1. Introduction

Since the definition of buried hill reservoir was introduced, a large number of buried hill oil and gas reservoirs have been explored and discovered, at present, large granite oil and gas reservoirs have been discovered in Vietnam, Libya, Venezuela, India and China's Bohai Basin [1–4], and their potential has attracted the attention of petroleum geologists around the world as various large granitic buried hill oil and gas reservoirs have achieved good development results. In recent years, as deepwater exploration in the north of the South China Sea continued to deepen, a high-quality granite buried hill gas reservoir was drilled and encountered in the YL area of the Qiongdongnan basin, resulting in a million cubic meters of high-quality gas production, creating a new record for buried hill gas testing capacity in China's seas [5,6]. However, the field faces more serious solids production problems, which seriously affects gas well production and reduces economic efficiency.

The solid production of gas wells will easily cause problems such as erosion of gas production equipment, sand stuck of downhole tools and blockage of valves, which will lead to sand accumulation in the wellbore, sand plugging of the reservoir, and a significant decrease in gas production of gas wells, thus affecting the development benefits of gas fields [7,8]. Early studies on the mechanism of solids production were limited to mechanical damage of reservoir rocks [9–11]; next, Vardoulakis et al. [12] proposed that solid production is related to the hydrodynamic instability controlled by both surface and internal fluids. Later, the solid production process is commonly described by scholars as two stages, the

initial stage is the stress equilibrium state of the rock surrounding the wellbore is broken, when the stress between the rock skeleton particles exceeds the tensile, compressive or shear strength of the rock itself, the formation rock undergoes mechanical destabilization and local damage, and the second stage is the damaged material is transported to the wellbore with fluid flow, causing substantial solid production from the formation [13–15]. The factors influencing the solid production can be summarized into four main classes: structural strength properties of reservoir rocks, physical properties and flow status of formation fluid, in-situ stress status and mining measures [16–19]. For gas reservoirs, studies by scholars have shown that reservoir characteristics are intrinsic to solid production in gas wells, and that solid production is more likely to occur in reservoirs with shallow burial and loose formations [20–23]. Gas flow rate in porous media is another major influencing factor for reservoir solid production, and the near-wellbore region of high-production gas wells generates a strong turbulent flow effect, which is one of the main factors causing solid production from the formation [23–25]. In addition, reservoir pressure depletion, high production pressure differential, water breakthrough, and frequent changes in work regime can also cause or aggravate the solid production [22,23,26,27].

However, these studies on solid production mainly focus on sandstone reservoirs, the characteristics of buried hill reservoirs are very different from sandstone [28–30], firstly, the composition of granite reservoir is different from that of sandstone, then granite matrix with greater strength, and granite reservoir with diverse storage space and more developed fractures. Studies have shown that the presence of fractures reduces reservoir strength and aggravates solid production [31–35], but the solid production mechanism of fractured granite reservoirs is still unclear and needs further study. To this end, the granite buried hill reservoir in the YL area of the Qiongdongnan Basin was used as an example to expose the reasons for solid production and clarify the mechanism. The research provides the basis and foundation for safe and efficient development of fractured granite reservoirs and for later measure selection and optimization.

2. Characteristics of Granite Reservoirs in YL Area of Qiongdongnan Basin

As shown in Figure 1, the results of granite reservoir composition slice microscopic identification in YL area of Qiongdongnan basin show that its main components are quartz (Qtz), plagioclase (Pl), amphibole (Am), biotite (Bt), etc., the high content of dark minerals proves that it is easily weathered and dissolved, which facilitates the formation of fractures and secondary dissolution. As shown in Figure 1, the quartz is mostly allotriomorphic granular, filled between the feldspar grains, and most of them contain crisscrossing irregular cracks due to the sudden cooling of the magma. The plagioclase is mostly hypidiotopic plate and granular, with varying degrees of claying and carbonation on the surface. The amphibole is mostly green, hypidiotopic-idiomorphic columnar, the biotite is mostly allotriomorphic-hypidiotopic plate, they are all partly transformed chloritic alteration.

According to previous study, the reservoir space of granite buried hill reservoir in YL area of Qiongdongnan Basin mainly includes dissolution pores and fractures [36,37]. The dissolution pores are mostly formed by the dissolution of minerals along the fractures, mainly due to the mineral particles in the rock were cut by fractures caused by the tectonic action, and partially or completely dissolved by fluids along the fractures at a later stage [37]. The fractures are mainly formed by tectonic stress during the formation of the granite buried hill reservoir, and are expanded and modified by dissolution at a later stage [36,37]. In addition, the fractures are mostly partially or completely filled with calcite, mica and iron, etc., and the unfilled fractures are less [37]. As shown in Figure 2a,b, there are clear fractures observed in typical core photographs and most are filled with calcite and mud, etc., the slice microscopic in Figure 2c also show that the granite reservoir in YL area is fracture developed.

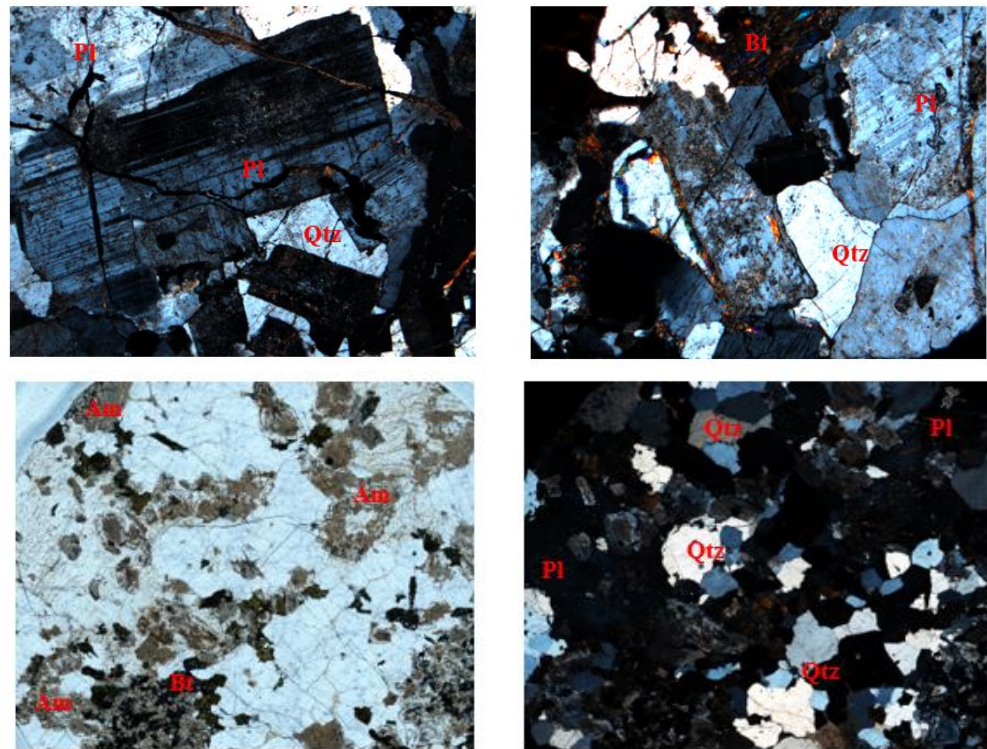


Figure 1. The slice microscopic identification of cores in the YL area of the Qiongdongnan Basin. (Qtz-quartz, Pl-plagioclase, Am-amphibole, Bt-biotite.).



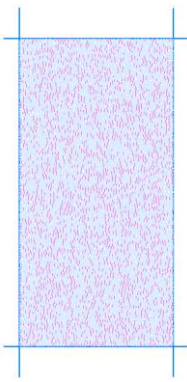
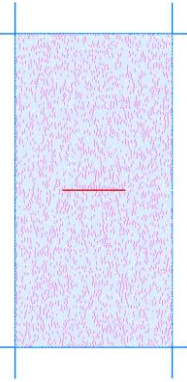
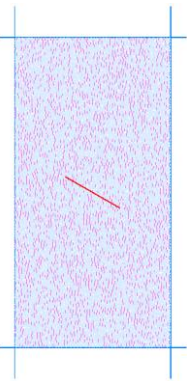
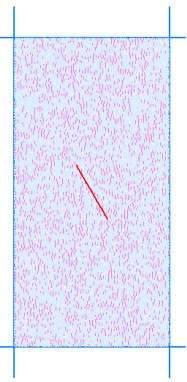
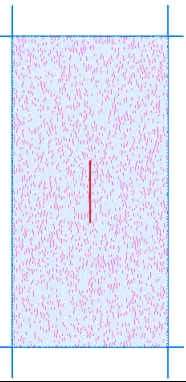
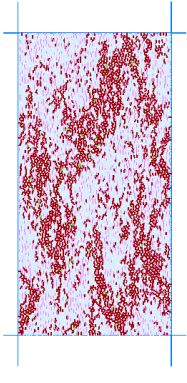
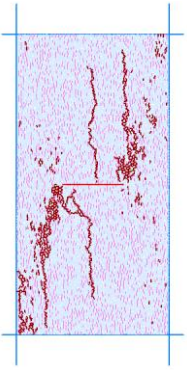
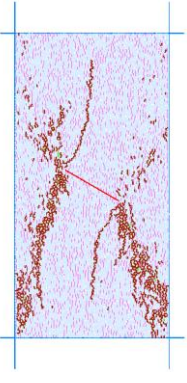
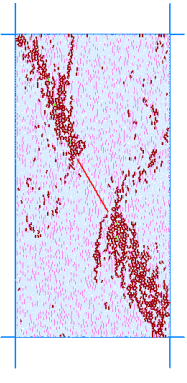
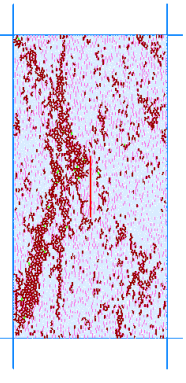
Figure 2. The typical core photographs and slice microscopic. (a,b) The core photographs, fracture developed, be partially filled; (c) Slice microscopic, fracture developed.

In order to analyze the influence of fractures on the solid production of granite reservoir, the influence of fracture on the mechanical properties of granite was firstly investigated. The PCF discrete element triaxial compression and Brazilian splitting simulation experiments were conducted on granite samples with prefabricated fractures at different angles due to there are multi-angle fractures in the reservoir.

The size of triaxial compression experimental model was a standard core sample with radius $r = 25$ mm and height $h = 100$ mm, and a single prefabricated fracture is added to the experimental model, the length of the fracture is 20 mm and the angles are 0° , 30° , 60° , and 90° , respectively. After simulated by triaxial compression experiments, the failure characteristics of the rock samples are shown in Table 1, and the complete stress-strain curves and the number of cracks are shown in Figure 3. When there is no prefabricated fracture, the rock sample reaches the compressive strength of 158 MPa, forming a macroscopic failure plane, with the main failure plane developing at an approximate angle of 60° to the horizontal plane, the overall number of cracks is larger, and the micro-cracks are dominated by tensile cracks. As shown in Figure 3a, when prefabricated fracture is present, the compressive strength is lower than that of the sample without fracture, and the compressive strength decreases as the prefabricated fracture angle increases. The lowest compressive strength is 70.8 MPa when 0° fracture is present, which is 45% lower than that of the sample without

fracture. The microcracks develop earlier in the samples with prefabricated fracture, as shown in Figure 3b, the microcracks started to develop at 0.1% strain for the sample with 0° prefabricated fracture, and at 0.2% strain for the sample without prefabricated fracture.

Table 1. The failure characteristics of granite by triaxial compression simulation.

The Angle of Prefabricated Fracture	No Prefabricated Fracture	0°	30°	60°	90°
Experimental model					
Failure characteristic					

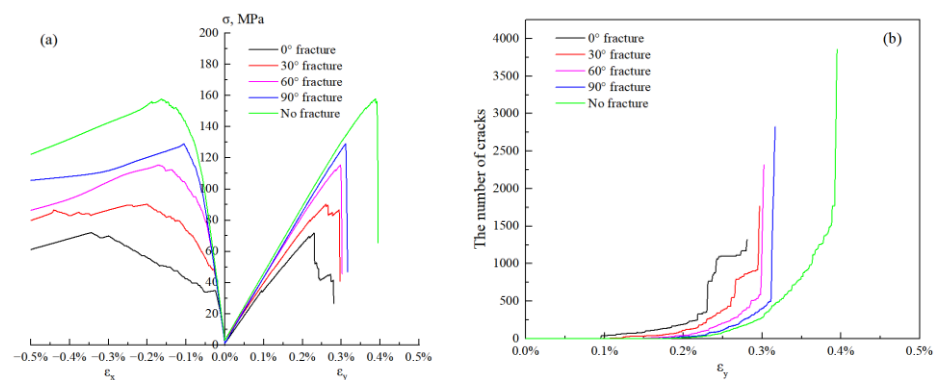
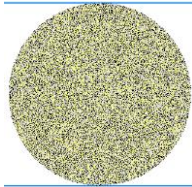
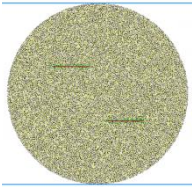
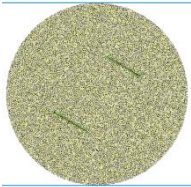
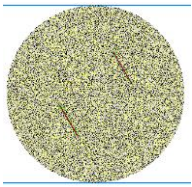
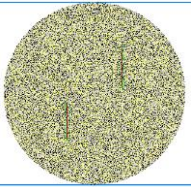
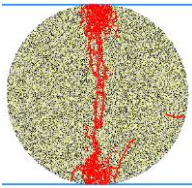
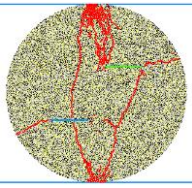
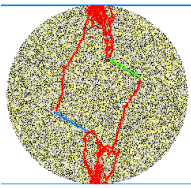
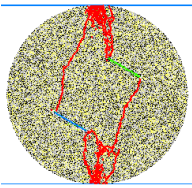
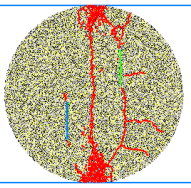


Figure 3. (a) The complete stress-strain curves and (b) the number of cracks of prefabricated fracture samples with different angles under triaxial compression.

The size of the Brazilian splitting experimental model was a standard core sample with radius $r = 25$ mm and thickness $h = 25$ mm, and two prefabricated fractures were added to the experimental model, the length of both fractures is 10 mm and the angles are 0°, 30°, 60° and 90°, respectively. After simulation by Brazilian splitting experiment, the failure forms of the rock samples are shown in Table 2, and the stress-strain curves and the number of cracks are shown in Figure 4. When there is no prefabricated fracture, the

rock sample reaches a tensile strength of 24.64 MPa, the main failure plane of the sample is relatively flat and is vertically to the wall, and the microcracks are mainly tensile cracks. As shown in Figure 4a, when there are prefabricated fractures, the tensile strength is lower than that of the samples without fractures, and the tensile strength first decreases and then increases as the prefabricated fracture angle increases. The lowest tensile strength was 12.41 MPa in the sample with 30° fractures, which was 50% lower than that of the samples without fracture. The microcracks develop earlier when there are prefabricated fractures, as shown in Figure 4b, the microcracks started to develop at 0.35% strain for the sample with 30° fractures, and at 0.45% strain for the sample without prefabricated fracture.

Table 2. The failure characteristics of granite by Brazilian splitting simulation.

The Angle of Prefabricated Fracture	No Prefabricated Fracture	0°	30°	60°	90°
Experimental model					
Failure characteristic					

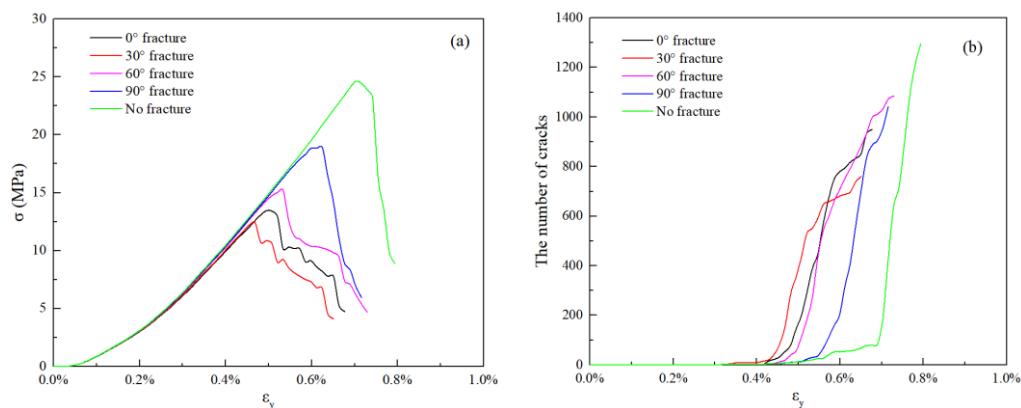


Figure 4. (a) The stress-strain curves and (b) the number of cracks of prefabricated fracture samples with different angles under Brazilian splitting.

In summary, the existence of fractures will reduce both the compressive strength and tensile strength of granite, and make microfractures develop earlier and rock sample failure easier.

3. Solid Production Model and Evaluation Method for Fractured Granite Reservoirs

According to the characteristics of granite buried hill reservoir in YL area of Qiongdongnan basin and the influence of fractures on the strength properties of the reservoir, as well as scholars' research on the solid production of fractured dense sandstone [31–35], the mode of solid production of granite buried hill reservoir can be divided into three modes: shedding of fracture filling and solid particles on the fracture wall, shear slip failure along the fracture, and shear failure of granite matrix.

3.1. Shedding of Fracture Filling and Solid Particles on the Fracture Wall

As shown in Figure 2, the fractures in the granite buried hill reservoir in the YL area are developed and mostly partially or completely filled with calcite and mud, etc. These fillings and the loose solid particles at the fracture wall have a weak cementation with the matrix rock, and when the gas flows in the fracture at high speed, it exerts a drag force on them. When the drag force exceeds their adhesion force, i.e., the gas flow rate in the fracture of a high-production gas well exceeds the threshold flow rate, the solid particles will be broken under the action of the drag force, leading to the shedding of fracture filling and solid particles on the fracture wall. The shed solid particles are transported with the fluid in the fracture, continuously hitting and flaking the wall, further promoting more solid particles to be shedding and forming solid production [34,35]. The closer the wellbore, the greater the flow rate of gas, and the greater the risk of shedding of fracture filling and solid particles on the fracture wall. If we can ensure that the solid particles on the fracture wall near the wellbore are not shed, the solid particles on the fracture wall in the reservoir are also less likely to be shed.

The cores of YL area in Qiongdongnan basin were selected and the high-speed gas injection experiments were conducted after fracturing by Brazilian splitting method. Where, N₂ with a purity of 99.9% is used for the gas injection. The injection rate is 100 mL/min. By testing the height of the contour line of the fracture wall before and after the experiment, it was found that the contour line of the fracture wall was significantly reduced, which indicated that the fracture wall under gas drag stress occurred obvious solid particle shedding, as shown in Figure 5.

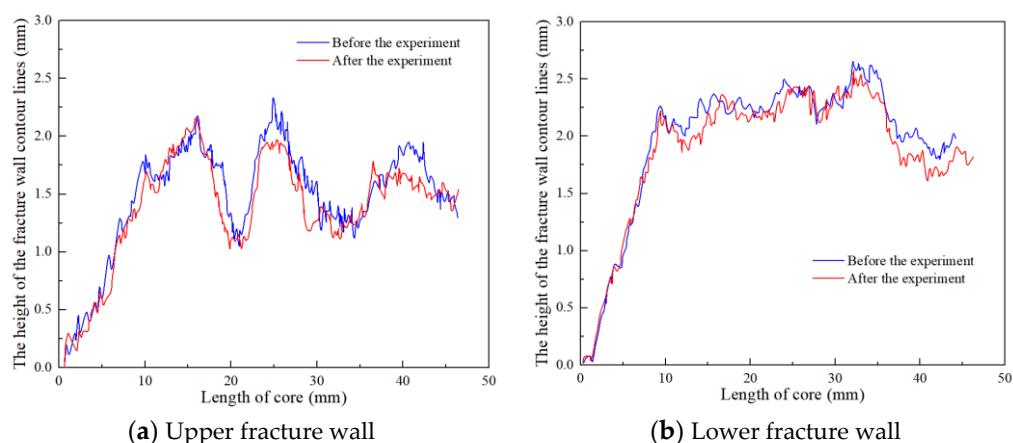


Figure 5. The comparison of the height of the fracture wall contour lines of the fracture core samples before and after the experiment.

3.2. Shear Slip Failure along the Fracture

The fractures are developed in granite reservoirs in the YL area of the Qiongdongnan Basin, and the existence of fractures will reduce both the compressive strength and tensile strength of granite, as shown in Figures 2–4. If the production or testing pressure difference is too large, the granite reservoir will easily failure, and then the fractures will gradually expand and connect to form solid small pieces, that will be transported to the wellbore with gas flow.

When analyzing the stress on the fracture plane, the well bore right angle coordinate system, the in-situ stress coordinate system, and the fracture plane coordinate system do not coincide with the global coordinate system, so the conversion between coordinate systems is necessary. The in-situ stress coordinate system and fracture plane coordinate system are first converted into the well bore right angle coordinate system, then the well bore right angle coordinate system is converted into the column coordinate system, and finally the failure is judged according to the rock stress state around the fracture combined with the strength criterion. Define the following coordinate systems: (1) global coordinate

system (X_e, Y_e, Z_e); (2) in-situ stress coordinate system (X_s, Y_s, Z_s); (3) fracture plane coordinate system (X_w, Y_w, Z_w); (4) well bore right angle coordinate system (X_b, Y_b, Z_b); (5) well bore column coordinate system (r, θ).

Figure 6 represents the relationship between the global coordinate system and the in-situ stress coordinate system. In the global coordinate system, X_e points to direct north, Y_e to direct west, and Z_e to direct vertical. In the in-situ stress coordinate system, X_s points to the horizontal minimum stress direction, Y_s points to the horizontal maximum stress direction, and Z_s points to the overburden pressure direction. The conversion relationship between the two coordinate systems is represented by α_s, β_s . First rotate around the Z_e axis by an angle of α_s , then rotate around the Y_s axis by an angle of β_s . In general, $\beta_s = 0$. However, in areas where the geomorphology is particularly complex, the overburden pressure may also slope at a certain angle. The in-situ stress tensor σ_{ics} is converted from the in-situ stress coordinate system to the global coordinate system, and the conversion matrix can be expressed in Equation (1).

$$\sigma_{ics-ecs} = E^T \times \sigma_{ics} \times E = \begin{bmatrix} \sigma_{xx}^e & \tau_{xy}^e & \tau_{xz}^e \\ \tau_{yx}^e & \sigma_{yy}^e & \tau_{yz}^e \\ \tau_{zx}^e & \tau_{zy}^e & \sigma_{zz}^e \end{bmatrix} \tag{1}$$

where,

$$E = \begin{bmatrix} \cos \beta_s & 0 & -\sin \beta_s \\ 0 & 1 & 0 \\ \sin \beta_s & 0 & \cos \beta_s \end{bmatrix} \begin{bmatrix} \cos \alpha_s & \sin \alpha_s & 0 \\ -\sin \alpha_s & \cos \alpha_s & 0 \\ 0 & 0 & 1 \end{bmatrix} = \begin{bmatrix} \cos \alpha_s \cos \beta_s & \sin \alpha_s \cos \beta_s & -\sin \beta_s \\ -\sin \alpha_s & \cos \alpha_s & 0 \\ \cos \alpha_s \sin \beta_s & \sin \alpha_s \sin \beta_s & \cos \beta_s \end{bmatrix}$$

$$\sigma_{ics} = \begin{bmatrix} \sigma_h & 0 & 0 \\ 0 & \sigma_H & 0 \\ 0 & 0 & \sigma_V \end{bmatrix}$$

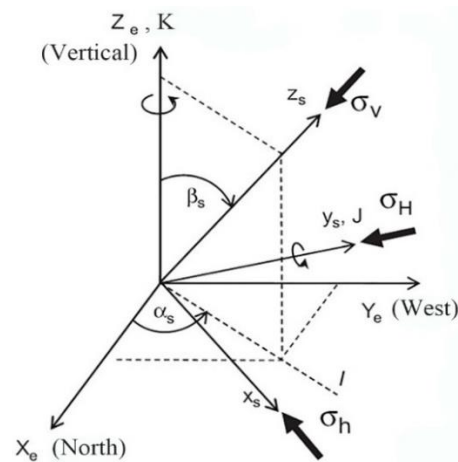


Figure 6. The conversion relationship between global coordinate system and in-situ stress coordinate system.

Figure 7 represents the relationship between the global coordinate system and the well bore right angle coordinate system. In the well bore right angle coordinate system, Z_b indicates the direction of the well bore axial, Y_b indicates the direction of the lateral normal, and X_b indicates the direction of the lower normal. The conversion relationship between the two coordinate systems is represented by α_b, β_b . First rotate around the Z_e axis by an angle α_b , then rotate around the Y_b axis by an angle β_b . where α_b is the azimuth between the well bore and direct north, β_b is the well slope angle. Convert the in-situ stress

tensor $\sigma_{ics-ecs}$, which has been converted to the global coordinate system, to the well bore right angle coordinate system as follows:

$$\sigma_{ecs-ics} = B \times \sigma_{ics-ecs} \times B^T = \begin{bmatrix} \sigma_{xx}^b & \tau_{xy}^b & \tau_{xz}^b \\ \tau_{yx}^b & \sigma_{yy}^b & \tau_{yz}^b \\ \tau_{zx}^b & \tau_{zy}^b & \sigma_{zz}^b \end{bmatrix} \quad (2)$$

where,

$$B = \begin{bmatrix} \cos \beta_b & 0 & -\sin \beta_b \\ 0 & 1 & 0 \\ \sin \beta_b & 0 & \cos \beta_b \end{bmatrix} \begin{bmatrix} \cos \alpha_b & \sin \alpha_b & 0 \\ -\sin \alpha_b & \cos \alpha_b & 0 \\ 0 & 0 & 1 \end{bmatrix} = \begin{bmatrix} \cos \alpha_b \cos \beta_b & \sin \alpha_b \cos \beta_b & -\sin \beta_b \\ -\sin \alpha_b & \cos \alpha_b & 0 \\ \cos \alpha_b \sin \beta_b & \sin \alpha_b \sin \beta_b & \cos \beta_b \end{bmatrix}$$

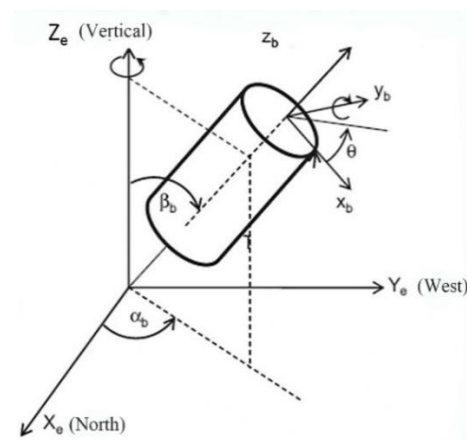


Figure 7. The conversion relationship between global coordinate system and well bore right angle coordinate system.

Figure 8 represents the relationship between the global coordinate system and the fracture plane coordinate system. In the fracture plane coordinate system, Z_w indicates the direction of upper inclination of the formation, Y_w indicates the direction of the formation, and X_w indicates the normal direction of the stratification plane. The conversion relationship between the two coordinate systems is represented by α_w, β_w . First rotate around the Z_e axis by an angle of α_w , then rotate around the Y_w axis by an angle of $90 - \beta_w$. Where, α_w is the angle between the projection of X_w on the horizontal plane and X_e , and β_w is the dip angle of the stratification plane. The conversion matrix between the global coordinate system and the fracture plane coordinate system can be expressed by Equation (3).

$$W = \begin{bmatrix} \cos(90 - \beta_w) & 0 & -\sin(90 - \beta_w) \\ 0 & 1 & 0 \\ \sin(90 - \beta_w) & 0 & \cos(90 - \beta_w) \end{bmatrix} \begin{bmatrix} \cos \alpha_w & \sin \alpha_w & 0 \\ -\sin \alpha_w & \cos \alpha_w & 0 \\ 0 & 0 & 1 \end{bmatrix} = \begin{bmatrix} \cos \alpha_w \sin \beta_w & \sin \alpha_w \sin \beta_w & \cos \beta_w \\ -\sin \alpha_w & \cos \alpha_w & 0 \\ -\cos \alpha_w \cos \beta_w & \sin \alpha_w \cos \beta_w & \sin \beta_w \end{bmatrix} \quad (3)$$

Figure 9 represents the conversion relationship between well bore right angle coordinate system and well bore column coordinate system with the following transformation matrix.

$$C = \begin{bmatrix} \cos \theta & \sin \theta & 0 \\ -\sin \theta & \cos \theta & 0 \\ 0 & 0 & 1 \end{bmatrix} \quad (4)$$

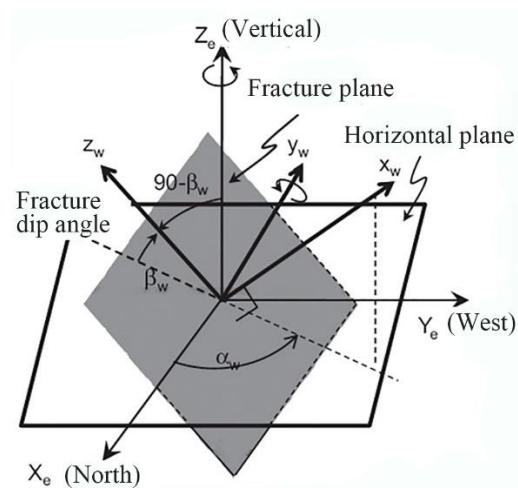


Figure 8. The conversion relationship between global coordinate system and fracture plane coordinate system.

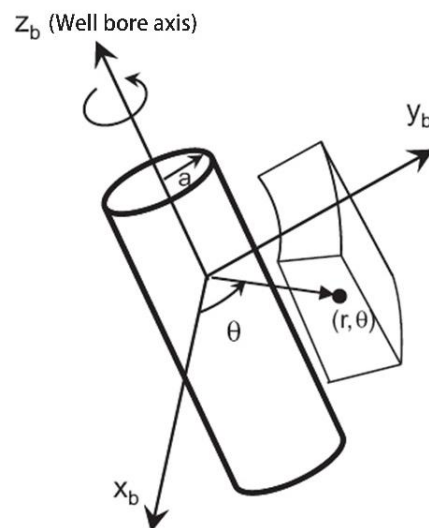


Figure 9. The conversion relationship between well bore right angle coordinate system and well bore column coordinate system.

After calculating and obtaining the stress state on the fracture plane, the Mohr-Coulomb shear failure criterion is used to adjudge the failure of the fracture plane [38–40].

$$\tau = C + \sigma \tan \phi \quad (5)$$

where, τ is the shear stress; σ is the normal positive stress; C is the cohesion; ϕ is the internal friction angle.

The relative magnitudes of in-situ stresses and the tectonic action are closely related. Based on Anderson's theory between faulting regime and the relative magnitudes of in-situ stresses [41], for normal faulting regime, the relative magnitudes of the three principal stresses are:

$$\sigma_v > \sigma_H > \sigma_h$$

For thrust faulting regime, the relative magnitudes of the three principal stresses are:

$$\sigma_H > \sigma_h > \sigma_v$$

For strike-slip faulting regime, the relative magnitudes of the three principal stresses are:

$$\sigma_H > \sigma_v > \sigma_h$$

where, σ_v is pressure of upper layer, σ_H is maximum horizontal stress, σ_h is minimum horizontal stress.

The YL area of Qiongdongnan basin is normal faulting regime [5,6], and the relative magnitudes of the three principal stresses are: $\sigma_v > \sigma_H > \sigma_h$. Using the above method, the risk of failure was calculated for fractures at different angles under this stress pattern, as shown in Figure 10, the color value represents the slip risk of the fracture, the larger the value, the greater the slip risk of the fracture. In addition, the value is greater than 1 means the fracture is slip state, otherwise it is in stable state. As can be seen from Figure 10, the high-angle fractures have a greater risk of failure during testing or production.

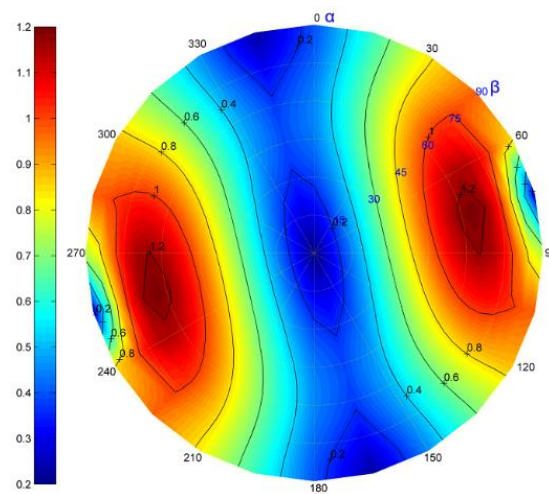


Figure 10. The risk of failure for fractures at different angles (where, α represents the fracture direction, β represents the fracture dip angle, the color value represents the slip risk of the fracture).

3.3. Shear Failure of Granite Matrix

Granite reservoir in YL area of Qiongdongnan basin granite reservoir is a high production gas well, high speed flow of gases in porous media generates additional pressure, Wang et al. [24] and Ong et al. [25] demonstrated that non-Darcy flow is one of the main factors causing formation solid production in high-producing gas wells. Based on this, the comparison of pore pressure gradient between non-Darcy flow and Darcy flow and the pore pressure distribution surrounding the wellbore are calculated. As shown in Figures 11 and 12, high speed flow of gases in porous media will generate higher pore pressure gradient, and the pressure gradient in the near wellbore increases sharply as the pressure at the bottom of the well decreases.

A model for calculating the stress state surrounding the wellbore during the testing of high-production gas wells was established by considering the additional stress of high-speed flow of gases in porous media, and combined with the Mohr-Coulomb criterion to evaluate the shear failure of the granite matrix.

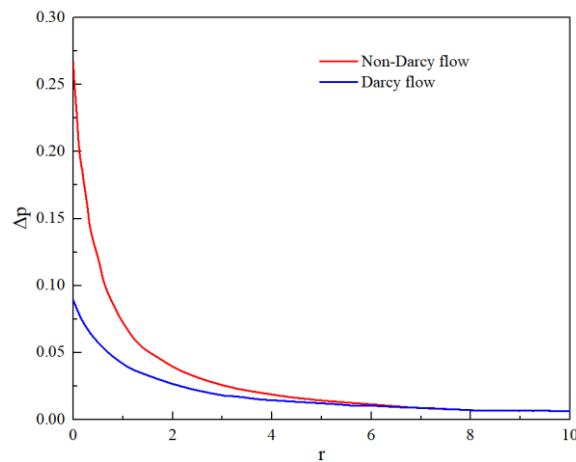


Figure 11. The comparison of pore pressure gradient of non-Darcy flow and Darcy flow.

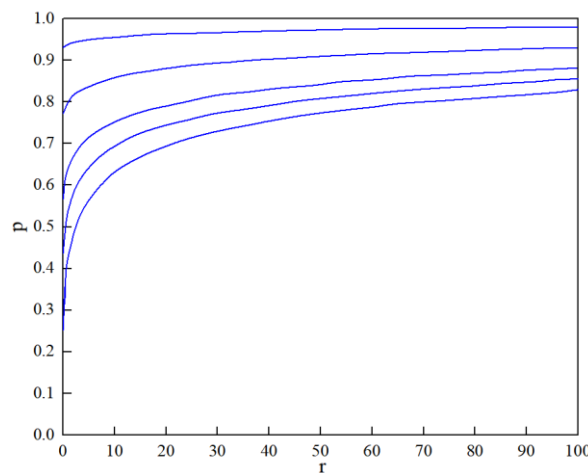


Figure 12. Pore pressure distribution surrounding the wellbore for high-speed flow of gases in porous media.

The formation stress surrounding the wellbore during high-pressure gas reservoir testing is influenced by the far-field stress and formation fluid pressure distribution, as shown in Figure 13. Assuming a far-field stress of σ_{r0} and a far-field formation fluid pressure of P_0 , the dimensionless stress surrounding the wellbore is [42,43]:

$$\begin{aligned} \sigma_r &= \frac{r_e^2(r^2-1)Y+(r_e^2-r^2)S}{r^2(r_e^2-1)} + \frac{2\eta}{r^2} \left[\int_1^r r' \Delta p(r') dr' - \frac{r^2-1}{r_e^2-1} \int_1^{r_e} r' \Delta p(r') dr' \right] \\ \sigma_\theta &= \frac{r_e^2(r^2+1)Y-(r_e^2+r^2)S}{r^2(r_e^2-1)} + 2\eta \Delta p(r) - \frac{2\eta}{r^2} \left[\int_1^r r' \Delta p(r') dr' + \frac{r^2+1}{r_e^2-1} \int_1^{r_e} r' \Delta p(r') dr' \right] \\ \sigma_z &= \chi + 2v_{fr} \frac{Y-S}{r_e^2-1} + 2\eta \Delta p(r) - 4\eta \frac{v_{fr}}{r_e^2-1} \int_1^{r_e} r' \Delta p(r') dr' \end{aligned} \quad (6)$$

where, $\Delta p(r) = p(r) - 1$, $Y = \sigma_{r0}/P_0 (> 1)$, $S = P_{wf}/P_0 (< 1)$, $\chi = \sigma_v/P_0$, $\eta = \frac{\alpha_B(1-2v_{fr})}{2(1-v_{fr})}$ ($0 \leq \eta \leq 0.5$) is gas flow coefficient in porous media, $\alpha_B (< 1)$ is Biot coefficient, v_{fr} ($0 < v_{fr} \leq 0.5$) is the rock Poisson's ratio.

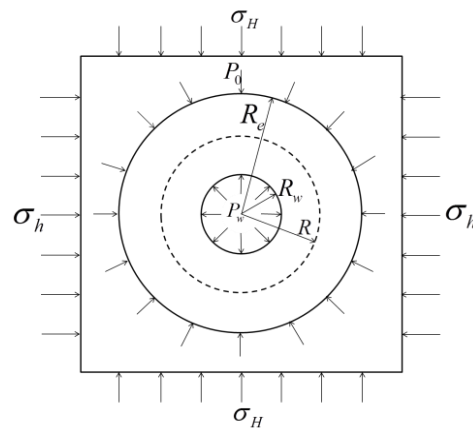


Figure 13. The schematic of stress state surrounding the wellbore during testing of high-pressure gas reservoirs.

All the following variables are dimensionless variables, so the effective stress in the rock surrounding the wellbore is:

$$\begin{aligned}
 \sigma'_r &= \sigma_r - \alpha_B p(r) = \frac{r_e^2(r^2-1)Y+(r_e^2-r^2)S}{r^2(r_e^2-1)} - \alpha_B p(r) \\
 &\quad + \frac{2\eta}{r^2} [\int_1^r r' \Delta p(r') dr' - \frac{r^2-1}{r_e^2-1} \int_1^{r_e} r' \Delta p(r') dr'] \\
 \sigma'_\theta &= \sigma_\theta - \alpha_B p(r) = \frac{r_e^2(r^2+1)Y-(r_e^2+r^2)S}{r^2(r_e^2-1)} - \alpha_B p(r) + 2\eta \Delta p(r) \\
 &\quad - \frac{2\eta}{r^2} [\int_1^r r' \Delta p(r') dr' + \frac{r^2+1}{r_e^2-1} \int_1^{r_e} r' \Delta p(r') dr'] \\
 \sigma'_z &= \sigma_z - \alpha_B p(r) = \chi + 2\nu_{fr} \frac{Y-S}{r_e^2-1} - \alpha_B p(r) + 2\eta \Delta p(r) - 4\eta \frac{\nu_{fr}}{r_e^2-1} \int_1^{r_e} r' \Delta p(r') dr'
 \end{aligned}
 \tag{7}$$

Assuming that rock failure follows the Mohr-Coulomb criterion, the effective stress can be expressed as:

$$\sigma'_1 - \sigma'_3 \cot^2(\pi/4 - \phi/2) = 2C \cot(\pi/4 - \phi/2)
 \tag{8}$$

where, σ'_1 is the maximum effective principal stress, σ'_3 is the minimum principal stress, C (c/p_0) is the dimensionless rock cohesion, and ϕ is the rock internal friction angle.

The formation is assumed to be a homogeneous, linearly elastic and porous material, and the rock surrounding the wellbore is considered to be in a plane strain. On the basis of Equation (7), the effective stress of the rock surrounding the wellbore under the flows action in porous media is obtained according to the elastic mechanics theory as:

$$\begin{aligned}
 \sigma'_r &= \sigma_r - \alpha_B p(r) = \frac{A}{2} \left(\frac{r_e^2}{r_e^2-1} - \frac{r_e^2}{(r_e^2-1)r^2} \right) + \frac{(r_e^2-r^2)S}{r^2(r_e^2-1)} + \\
 &\quad \frac{B}{2} \left(\frac{r_e^2(r_e^4+r_e^2+4)}{(r_e^2-1)^3} + \frac{3r_e^4(r_e^2+1)}{(r_e^2-1)^3 r^4} - 4 \frac{r_e^2(r_e^4+r_e^2+1)}{(r_e^2-1)^3 r^2} \right) \cos 2\theta \\
 &\quad + \frac{2\eta}{r^2} [\int_1^r r' \Delta p(r') dr' - \frac{r^2-1}{r_e^2-1} \int_1^{r_e} r' \Delta p(r') dr'] - \alpha_B p(r) \\
 \sigma'_\theta &= \sigma_\theta - \alpha_B p(r) = \frac{A}{2} \left(\frac{r_e^2}{r_e^2-1} + \frac{r_e^2}{(r_e^2-1)r^2} \right) - \frac{(r_e^2+r^2)S}{r^2(r_e^2-1)} \\
 &\quad - \frac{B}{2} \left(\frac{r_e^2(r_e^4+r_e^2+4)}{(r_e^2-1)^3} + \frac{3r_e^4(r_e^2+1)}{(r_e^2-1)^3 r^4} - \frac{12r_e^2 r^2}{(r_e^2-1)^3} \right) \cos 2\theta \\
 &\quad + 2\eta \Delta p(r) - \frac{2\eta}{r^2} [\int_1^r r' \Delta p(r') dr' + \frac{r^2+1}{r_e^2-1} \int_1^{r_e} r' \Delta p(r') dr'] - \alpha_B p(r)
 \end{aligned}
 \tag{9}$$

where, $A = \frac{\sigma_H + \sigma_h}{p_0}$, $B = \frac{\sigma_H - \sigma_h}{p_0}$, σ_H is the maximum horizontal stress, σ_h is the minimum horizontal stress, θ is the angle between the radial direction at a point surrounding the wellbore and the maximum horizontal stress.

Cause:

$$H(r) = \frac{r_e^2(r_e^4 + r_e^2 + 4)}{(r_e^2 - 1)^3} + \frac{3r_e^4(r_e^2 + 1)}{(r_e^2 - 1)^3 r^4} - \frac{12r_e^2 r^2}{(r_e^2 - 1)^3}
 \tag{10}$$

when $1 \leq r \leq r_e$, $\frac{dH(r)}{dr} < 0$, then,

$$H(r) \geq H(r_e) = \frac{r_e^6 - 11r_e^4 + 7r_e^2 + 3}{(r_e^2 - 1)^3} \quad (11)$$

when $r_e > 3.3$ (Generally $r_e \gg 1$),

$$H(r) > 0 \quad (12)$$

It can be seen that $\sigma_{\theta'}$ is minimum in the direction of maximum horizontal stress and maximum in the direction of minimum horizontal stress. Next,

$$\begin{aligned} & (\sigma_{\theta'} - \cot^2(\pi/4 - \varphi/2)\sigma_r') \Big|_{r=1, \alpha_B=1} \\ & = \left(\frac{A}{1-\frac{1}{r_e^2}} - 2\eta \right) - \left(\frac{r_e^2+1}{r_e^2-1} + 1 - 2\eta \right) D - 2\eta \bar{p} - BH(1) \cos 2\theta \end{aligned} \quad (13)$$

Due to $0 \leq \eta \leq 0.5$, it can be seen that $\sigma_{\theta'} - \cot^2(\pi/4 - \varphi/2)\sigma_r'$ on the wellbore is the smallest in the direction of the maximum horizontal stress and the largest in the direction of the minimum horizontal stress, i.e., the rock surrounding the wellbore in the direction of the minimum horizontal principal stress is first to be failed.

The reservoir rocks in YL area of Qiongdongnan Basin were selected for strength analysis, and it was found that the compressive strength of granite was generally higher than 100 MPa and the elastic modulus was above 30 GPa, which shows that the strength of granite matrix is higher and the possibility of matrix shear failure during the test period is less.

4. Conclusions

The granite buried hill gas reservoir in YL area of Qiongdongnan basin faces a serious problem of solid production, which seriously affects gas well production and reduces economic benefits; however, the solid production mechanism of fractured granite reservoirs is still unclear. In this study, the reasons for solid production were revealed and the mechanism was clarified based on the analysis of geological and mechanical characteristics of the granite buried hill reservoir. The research provides the basis and foundation for safe and efficient development of fractured granite reservoirs and for later measure selection and optimization.

(1) The granite buried hill reservoir has a high content of dark minerals, and the fractures are developed and mostly partially or completely filled with calcite and mud, etc. These fillings and the loose solid particles at the fracture wall have a weak cementation with the matrix rock. In addition, the existence of fractures will reduce both the compressive strength and tensile strength of granite.

(2) The solid production of fractured granite reservoirs can be divided into three modes: shedding of fracture filling and solid particles on the fracture wall, shear slip failure along the fracture, and shear failure of granite matrix.

(3) Take the YL area in the Qiongdongnan Basin as an example, the solid production of fractured granite reservoir is mainly based on shedding of fracture filling and solid particles on the fracture wall and shear slip failure along the fracture, the possibility of shear failure of granite matrix is less.

(4) The closer the wellbore, the greater the risk of shedding of fracture filling and solid particles on the fracture wall. The high-angle fractures have a greater risk of shear slip failure. In addition, the direction of the minimum horizontal principal stress is higher risk of solid production.

Author Contributions: Conceptualization, X.Z. and T.W.; methodology, X.Z.; validation, T.W., L.S. and L.D.; formal analysis, J.W.; investigation, L.L.; data curation, X.Z.; writing—original draft preparation, X.Z.; writing—review and editing, T.L.; supervision, T.W.; project administration, T.L.; funding acquisition, L.D. All authors have read and agreed to the published version of the manuscript.

Funding: This research was financially supported by the Innovation Capability Support Program of Shaanxi (grant number 2022KJXX-63), the Scientific Research Key Program Funded by Shaanxi Provincial Education Department (grant number 21JY036), the National Natural Science Foundation of China (No.5202010500).

Institutional Review Board Statement: Not applicable.

Informed Consent Statement: Not applicable.

Data Availability Statement: Not applicable.

Conflicts of Interest: The authors declare no conflict of interest.

References

1. Koning, T. Oil and gas production from basement reservoirs: Examples from Indonesia, USA and Venezuela. *Geol. Soc. Lond. Spec. Publ.* **2003**, *214*, 83–92. [[CrossRef](#)]
2. Micarelli, L.; Benedicto, A.; Wibberley, C.A.J. Structural evolution and permeability of normal fault zones in highly porous carbonate rocks. *J. Struct. Geol.* **2006**, *28*, 1214–1227. [[CrossRef](#)]
3. Huang, J.H.; Tan, X.F.; Cheng, C.J.; Li, Z.M.; Ma, L.J.; Zhang, H.L.; Wu, Y.X. Structural features of weathering crust of granitic basement rock and its petroleum geological significance: A case study of Basement weathering crust of Dongping Area in Qaidam Basin. *Earth Sci.* **2016**, *41*, 2041–2060.
4. Ye, T.; Wei, A.; Sun, Z.; Gao, K.; Cheng, Q. The reservoir characteristics and their significance for deliverability in metamorphic granite buried hill: A case study from the JZS oil field in the Liaodong Bay Basin, NE China. *Arab. J. Geosci.* **2019**, *12*, 1–9. [[CrossRef](#)]
5. You, L.; Xu, S.; Mao, X.; Zhong, J.; Jiao, Y.; Xiong, X. Reservoir Characteristics and Genetic Mechanisms of the Mesozoic Granite Buried Hills in the Deep-water of the Qiongdongnan Basin, Northern South China Sea. *Acta Geol. Sin.-Engl. Ed.* **2021**, *95*, 259–267. [[CrossRef](#)]
6. Ji, M.; Zeng, Q.; Yang, H.; Guo, S.; Zhong, K. Structural characteristics of central depression belt in deep-water area of the Qiongdongnan Basin and the hydrocarbon discovery of Songnan low bulge. *Acta Oceanol. Sin.* **2021**, *40*, 42–53. [[CrossRef](#)]
7. Song, Y.; Ranjith, P.G.; Wu, B. Development and experimental validation of a computational fluid dynamics-discrete element method sand production model. *J. Nat. Gas Sci. Eng.* **2020**, *73*, 103052. [[CrossRef](#)]
8. Li, X.; Yi, L.; Fan, Z. Sand Production of the Shale Gas Well in Different Production Periods: Structure and Component. *Energies* **2021**, *14*, 5588. [[CrossRef](#)]
9. Morita, N.; Whitfill, D.L.; Massie, I.; Knudsen, T.W. Realistic sand-production prediction: Numerical approach. *SPE Prod. Eng.* **1989**, *4*, 15–24. [[CrossRef](#)]
10. Vaziri, H.H. Theoretical analysis of stress, pressure, and formation damage during production. *J. Can. Pet. Technol.* **1988**, *27*, 880613. [[CrossRef](#)]
11. Perkins, T.K.; Weingarten, J.S. Stability and failure of spherical cavities in unconsolidated sand and weakly consolidated rock. In Proceedings of the SPE Annual Technical Conference and Exhibition, Houston, TX, USA, 2–5 October 1988. SPE-18244.
12. Vardoulakis, I.; Stavropoulou, M.; Papanastasiou, P. Hydro-mechanical aspects of the sand production problem. *Transp. Porous Media* **1996**, *22*, 225–244. [[CrossRef](#)]
13. Wu, B.; Tan, C.P.; Lu, N. Effect of water cut on sand production—An experimental study. *SPE Prod. Oper.* **2006**, *21*, 349–356. [[CrossRef](#)]
14. Eshiet, K.; Sheng, Y. Influence of rock failure behaviour on predictions in sand production problems. *Environ. Earth Sci.* **2013**, *70*, 1339–1365. [[CrossRef](#)]
15. Li, X.; Feng, Y.; Gray, K.E. A hydro-mechanical sand erosion model for sand production simulation. *J. Pet. Sci. Eng.* **2018**, *166*, 208–224. [[CrossRef](#)]
16. Veeken, C.A.M.; Davies, D.R.; Kenter, C.J.; Kooijman, A.P. Sand production prediction review: Developing an integrated approach. In Proceedings of the 1991 SPE Annual Technical Conference and Exhibition, Dallas, TX, USA, 6–9 October 1991; SPE 22792.
17. Van den Hoek, P.J.; Hertogh, G.M.M.; Kooijman, A.P.; De Bree, P.; Kenter, C.J.; Papamichos, E. A new concept of sand production prediction: Theory and laboratory experiments. *SPE Drill. Complet.* **2000**, *15*, 261–273. [[CrossRef](#)]
18. Rahmati, H.; Jafarpour, M.; Azadbakht, S.; Nouri, A.; Vaziri, H.; Chan, D.; Xiao, Y. Review of sand production prediction models. *J. Pet. Eng.* **2013**, *2013*, 864981. [[CrossRef](#)]
19. Cui, Y.; Nouri, A.; Chan, D.; Rahmati, E. A new approach to DEM simulation of sand production. *J. Pet. Sci. Eng.* **2016**, *147*, 56–67. [[CrossRef](#)]
20. Vriezen, P.B.; Spijker, A.; Van der Vlis, A.C. Erosion of perforation tunnels in gas wells. In Proceedings of the Fall Meeting of the Society of Petroleum Engineers of AIME, Dallas, TX, USA, 28 September–1 October 1975. SPE-5661.
21. Antheunis, D.; Vriezen, P.B.; Schipper, B.A.; Van der Vlis, A.C. Perforation collapse: Failure of perforated friable sandstones. In Proceedings of the SPE European Spring Meeting, Amsterdam, The Netherlands, 8–9 April 1976; SPE-5750.
22. Wang, X.; Yang, W.; Yang, H. The sanding mechanism and sanding critical drawdown calculation in loose sandstone. *Nat. Gas Ind.* **2009**, *29*, 72–75.

23. Zhong, B.; Ma, L.; Yang, Y.; Xia, C.; Li, J. Study on Sand Producing Mechanism of Gas Wells and Counter-Measures for Gas Reservoirs with Multilayer Sand. *Nat. Gas Ind.* **2004**, *24*, 89–92.
24. Wang, Z.; Peden, J.M.; Damasena, E.S.H. The prediction of operating conditions to constrain sand production from a gas well. In Proceedings of the SPE Production Operations Symposium, Oklahoma City, OK, USA, 7–9 April 1991. SPE-21681.
25. Ong, S.; Ramos, R.; Zheng, Z. Sand production prediction in high rate, perforated and open-hole gas wells. In Proceedings of the SPE International Symposium on Formation Damage Control, Lafayette, LA, USA, 23–24 February 2000. SPE-58721.
26. Morita, N.; Whitfill, D.L.; Fedde, O.P.; Lovik, T.H. Parametric study of sand-production prediction: Analytical approach. *SPE Prod. Eng.* **1989**, *4*, 25–33. [[CrossRef](#)]
27. Bruno, M.S.; Bovberg, C.A.; Meyer, R.F. Some influences of saturation and fluid flow on sand production: Laboratory and discrete element model investigations. In Proceedings of the SPE Annual Technical Conference and Exhibition, Denver, CO, USA, 6–9 October 1996; SPE-36534.
28. Hou, M.; Cao, H.; Li, H.; Chen, A.; Wei, A.; Chen, Y.; Wang, Y.; Zhou, X.; Ye, T. Characteristics and controlling factors of deep buried-hill reservoirs in the BZ19-6 structural belt, Bohai Sea area. *Nat. Gas Ind. B* **2019**, *6*, 305–316. [[CrossRef](#)]
29. Ye, T.; Niu, C.; Wei, A. Characteristics and genetic mechanism of large granitic buried-hill reservoir, a case study from PengLai oil field of Bohai Bay Basin, north China. *J. Pet. Sci. Eng.* **2020**, *189*, 106988. [[CrossRef](#)]
30. Dou, L.; Xiao, Y.; Gao, H.; Wang, R.; Liu, C.; Sun, H. The study of enhanced displacement efficiency in tight sandstone from the combination of spontaneous and dynamic imbibition. *J. Pet. Sci. Eng.* **2021**, *199*, 108327. [[CrossRef](#)]
31. Lee, H.; Jeon, S. An experimental and numerical study of fracture coalescence in pre-cracked specimens under uniaxial compression. *Int. J. Solids Struct.* **2011**, *48*, 979–999. [[CrossRef](#)]
32. Jiang, J.; Li, X. Sand Production Mechanism Analysis of Deep Tight Sandstone Gas Reservoir in Keshen Block. *IOP Conf. Ser. Earth Environ. Sci.* **2021**, *781*, 022022. [[CrossRef](#)]
33. Yang, X.; Jin, X.; Zhang, Y.; Yin, Q.; McLennan, J.; Dai, C.; Fan, W.; Xiao, Y. Investigating the fundamental mechanisms governing solid production in superdeep hot tight gas reservoirs and exploring potential solutions. In Proceedings of the SPE Annual Technical Conference and Exhibition, Dubai, United Arab Emirates, 26–28 September 2016; SPE-181731.
34. Zhang, D.; Kang, Y.; You, L.; Zhou, Z.; Zhu, J.; Li, J. Mechanisms of sand production from fracture wall and its effect on stress sensitivity in ultra-deep tight sandstone reservoirs. *Pet. Geol. Recovery Effic.* **2017**, *24*, 72–78.
35. Sun, H.; Chang, B.; Zhang, J.; Zhang, J.; Wang, X.; Chen, B.; Liu, L. Causes of sand production and its influence on the output of fractured tight sandstone gas reservoirs: A case study on the Keshen Gas Field, Tarim Basin. *Nat. Gas Ind.* **2018**, *38*, 52–58.
36. Xu, S.L.; You, L.; Mao, X.L.; Zhong, J.; Wu, S.J. Reservoir characteristics and controlling factors of granite buried hill in Songnan Low Uplift, Qiongdongnan Basin. *Earth Sci.* **2019**, *44*, 2717–2728.
37. Li, H.; Wang, P.; Xu, S.; Liu, Y.; Wu, S.; Jiao, Y.; Xiong, X. Reservoir characteristics and controlling factors of Prepaleogene granite buried-hill in Songnan low uplift, Qiongdongnan Basin. *World Geol.* **2022**, *41*, 1–15.
38. Ismail, N.I.; Naz, M.Y.; Shukrullah, S.; Sulaiman, S.A. Mechanical earth modeling and sand onset production prediction for Well X in Malay Basin. *J. Pet. Explor. Prod. Technol.* **2020**, *10*, 2753–2758. [[CrossRef](#)]
39. Sanchez, E.C.M.; Cordero, J.A.R.; Roehl, D. Numerical simulation of three-dimensional fracture interaction. *Comput. Geotech.* **2020**, *122*, 103528. [[CrossRef](#)]
40. Wang, H.; Sharma, M.M. The role of elasto-plasticity in cavity shape and sand production in oil and gas wells. *SPE J.* **2019**, *24*, 744–756. [[CrossRef](#)]
41. Farsimadan, M.; Dehghan, A.N.; Khodaei, M. Determining the domain of in situ stress around Marun Oil Field’s failed wells, SW Iran. *J. Pet. Explor. Prod. Technol.* **2020**, *10*, 1317–1326. [[CrossRef](#)]
42. Fjaer, E.; Holt, R.M.; Horsrud, P.; Raaen, A.M. *Petroleum Related Rock Mechanics*, 2nd ed.; Elsevier: Amsterdam, The Netherlands, 2008; pp. 341–369.
43. Shabdirova, A.; Minh, N.H.; Zhao, Y. A sand production prediction model for weak sandstone reservoir in Kazakhstan. *J. Rock Mech. Geotech. Eng.* **2019**, *11*, 760–769. [[CrossRef](#)]